Research Article Vol. 33, No. 15 / 28 Jul 2025 / Optics Express 31195

Optics EXPRESS

MOCVD-grown InAs/InP quantum dot lasers with low threshold current

ZHAO YAN,[1] SHANGFENG LIU,[1] BOGDAN-PETRIN RATIU,[1] KA MING WONG,[1] HAOTIAN ZENG,[2] YANGQIAN WANG,[2] JAE-SEONG PARK,[2] HUI JIA,[2] MINGCHU TANG,[2] HUIYUN LIU,[2] PETER M. SMOWTON,[1] AND QIANG LI[1,*]

[1] *School of Physics and Astronomy, Cardiff University, Cardiff CF24 3AA, UK*
[2] *Department of Electronic and Electrical Engineering, University College London, London WC1E 7JE, UK*
[*] *LiQ44@cardiff.ac.uk*

Abstract: We report low-threshold-current, high-yield InAs/InP quantum dot lasers in the C- and L-bands grown by metal-organic chemical vapor deposition (MOCVD). By optimizing the epitaxial growth conditions, including the introduction of a GaAs interfacial layer, we achieved more in-plane symmetric quantum dots with improved optical quality. Deep-etched ridge waveguide lasers with a 4 µm ridge width and top–top metal contacts were fabricated and characterized under pulsed injection. Low threshold currents of 17 mA and 28 mA were obtained for cavity lengths of 300 µm and 1000 µm, respectively. Temperature-dependent measurements showed lasing sustained up to 120 °C with a characteristic temperature T_0 of 74.9 K below 90 °C.

1. Introduction

Long-wavelength semiconductor lasers operating in the C- and L-bands are critical light sources for long-haul optical fiber communications, high-speed data transmission, and eye-safe optical sensing applications [1–4]. To meet the rapidly growing demands for increased data capacity and scalable photonic integration, it is crucial to develop C- and L-band lasers exhibiting high performance and high manufacturing yield [5–7]. Currently, multi-quantum-well (MQW) lasers, such as quaternary InGaAsP on InP substrates, serve as commercial solutions for these wavelength bands and are typically realized using MOCVD. Compared with conventional two-dimensional quantum wells, zero-dimensional quantum dot (QD) active regions offer unique advantages arising from their highly localized carrier confinement and discrete density of states, enabling lasers with reduced threshold currents and improved temperature stability [8,9]. In the InAs/GaAs material system, QD lasers have demonstrated several performance benefits over their MQW counterparts, including insensitivity to on-chip optical reflections, superior optical frequency comb generation capability, and enhanced tolerance to crystalline defects [10–12]. Recent advances have shown that InAs/GaAs QD lasers grown on silicon substrates can achieve long operational lifetimes, facilitating their integration onto 300-mm silicon wafers [13–16]. Despite these successes, InAs/GaAs QD lasers are limited to emission in the O-band wavelength region. To harness the advantageous properties of QDs in the C- and L-bands, the InAs/InP based material system is yet to be fully exploited.

Growing high-quality InAs QDs on InP substrates presents different material challenges compared to the InAs/GaAs system. The lattice mismatch between InAs and InP (~3%) is smaller than that between InAs and GaAs (~7%), resulting in lower strain energy available during self-assembled QD formation [17]. This reduction in strain makes the growth of uniform, height-controlled QDs more challenging. Moreover, with decreased strain dominance, surface

#568365 https://doi.org/10.1364/OE.568365
Journal © 2025 Received 20 May 2025; revised 18 Jun 2025; accepted 20 Jun 2025; published 15 Jul 2025

Optics EXPRESS

reconstruction effects become increasingly significant. Consequently, the InAs/InP material system often favors elongated one-dimensional quantum dash structures aligned along the $[1\bar{1}0]$ crystallographic direction [18–20], rather than the preferred zero-dimensional QDs. To overcome these challenges, several approaches have been explored to grow InAs/InP QDs, mostly using molecular beam epitaxy (MBE) [21–28]. Low-threshold InAs/InP QD lasers recently have been demonstrated by MBE [29], highlighting the potential of carefully engineered QDs in this material system. By comparison, reports of MOCVD-grown InAs/InP QD lasers remain relatively limited [30]. MOCVD offers advantages in low-cost manufacturing, scalability, and selective epitaxy on 300 mm silicon platforms, making it attractive for mass production and photonic integration [31–35].

In this study, we report the development of MOCVD-grown InAs/InP QD lasers exhibiting low threshold currents and high lasing yields. Through careful optimization of the epitaxial growth conditions and strain engineering, the QDs show efficient optical emission around the 1.55 µm wavelength band. Deeply etched ridge waveguide lasers were fabricated without any facet coatings. A 3D schematic of the laser structure, along with a cross-sectional scanning electron microscopy (SEM) image is presented in Fig. 1, showing the QD active region fully confined within the ridge cavity. Lasers with a ridge width of 4 µm exhibited low threshold currents of 17 mA for the 300-µm cavity and 28 mA for the 1000-µm cavity. High-temperature pulse lasing was achieved, with lasing demonstrated up to 120 °C. These results highlight the potential of MOCVD-grown InAs/InP QD lasers as high-performance, high-yield light source candidates for C- and L-band applications.

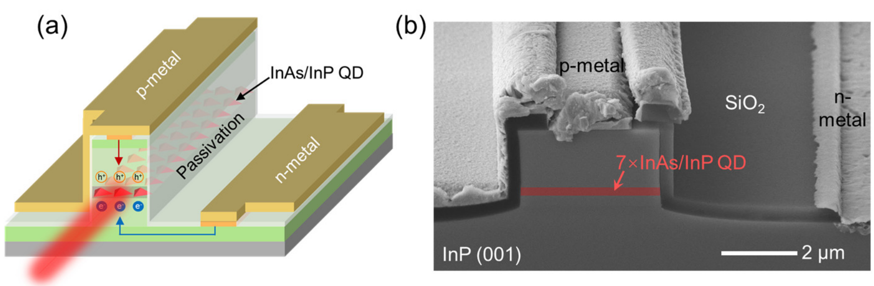

Fig. 1. (a) Schematic illustration of the deep-etched ridge laser structure, in which the InAs/InP QD active region is fully enclosed within the ridge cavity. (b) Cross-sectional SEM image from a 4 µm × 2000 µm laser device.

2. Experiment

We first investigated the growth of InAs/InP QDs on InP (001) n-type substrates using an Aixtron close-coupled showerhead (CCS) MOCVD system. Fig. 2(a) illustrates the complete laser structure, which consists of 7 layers of InAs QDs centrally located within the active region, embedded between the unintentionally-doped (UID) $In_{0.52}Al_{0.26}Ga_{0.22}As$ confinement layers. The structure also includes lightly doped n-type and p-type InP cladding layers, along with heavily doped n-InP and p-InGaAs contact layers. The total thickness of the epitaxial stack is approximately 4 µm. After the full laser structure was grown, the top surface was examined using atomic force microscopy (AFM). Figs. 2(b) and 2(c) show 10×10 µm^2 and 30×30 µm^2 AFM scans, respectively, taken after completing the full epitaxy. The surfaces exhibit a smooth morphology with RMS roughness values of approximately 0.12 nm and 0.14 nm, respectively. A clear step-flow pattern is observed along the [110] direction, as indicated by the white arrows in both images, indicating the high crystalline quality and uniformity of the grown layers.

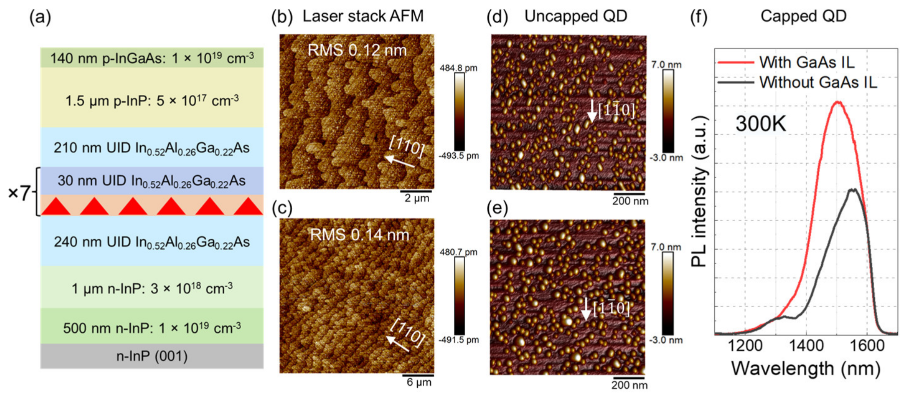

Fig. 2. (a) Schematic of the seven-layer InAs/InP QD laser structure. (b, c) AFM images of the wafer surface after full laser stack growth (10 µm × 10 µm and 30 µm × 30 µm, respectively), showing a step-flow morphology along the [110] direction. (d, e) AFM images of uncapped QDs grown without and with a 0.5 nm GaAs interfacial layer, respectively. Elongation along the [1$\bar{1}$0] direction is observed in (d) and effectively suppressed in (e). (f) Room-temperature PL spectra of capped QDs without and with the 0.5 nm GaAs interfacial layer with a pump power of 1.7 kW/cm^2.

To achieve uniform InAs/InP QDs and efficient photoluminescence (PL) emission in the 1.55 µm wavelength band, both the morphology of uncapped QDs and the optical quality of capped QDs were carefully optimized. The 240 nm $In_{0.52}Al_{0.26}Ga_{0.22}As$ barrier layer is nearly lattice-matched to InP. A dot-in-well (DWELL) structure was adopted to control the strain build-up, similar to those used in the O-band InAs/GaAs QD lasers [13].

The optimized growth sequence for the QD deposition was as follows: following the growth of the 240 nm InAlGaAs layer, the growth temperature was reduced to 460 °C. A 2 nm $In_{0.35}Ga_{0.65}As$ prelayer was then deposited to facilitate QD nucleation. This was followed by the deposition of 2.9 monolayers of InAs, after which a 30-second growth interruption was applied to promote dot formation. Subsequently, a 4 nm $In_{0.35}Ga_{0.65}As$ layer was deposited as the first cap layer, maintained at the same temperature. Finally, the temperature was ramped up to 560 °C to grow a 30 nm InAlGaAs second cap layer. To evaluate the growth quality, two sets of samples were prepared. The uncapped QD samples, without the two capping layers, were used to examine dot morphology. The capped samples, featuring the full DWELL structure and matching a single repeat unit from the 7-layer active region in Fig. 2(a), were used for PL measurements to assess optical performance.

The AFM image in Fig. 2(d) shows the surface morphology of the uncapped QDs. A dot density of 3.4×10^{10} cm^{-2} with an average height of 5.1 nm is determined. However, the InAs dots exhibit a noticeable elongation along the [1$\bar{1}$0] direction, as indicated by the white arrow in Fig. 2(d). This elongation is attributed to the limited strain during dot formation, which, coupled with surface reconstruction effects, tends to promote the evolution of quantum dash-like structures [17]. To mitigate this, the QD growth conditions were modified by replacing the original 2 nm $In_{0.35}Ga_{0.65}As$ prelayer with a composite layer consisting of 1.5 nm $In_{0.35}Ga_{0.65}As$ and a 0.5 nm GaAs interfacial layer (IL). The corresponding AFM image is shown in Fig. 2(e). Based on two 1×1 µm^2 AFM scans, the dot density was measured to be 3.0×10^{10} cm^{-2}, while the average dot height is slightly reduced to 4.9 nm. The dots now exhibit more in-plane symmetry with the elongation along the [1$\bar{1}$0] direction suppressed. There are some large dots with a density of approximately 1×10^9 cm^{-2}. As illustrated in Fig. 2(f), PL measurements of the single-layer capped QDs with the GaAs IL show an increase in PL intensity. The size dispersion of the dots

Optics EXPRESS

remains relatively broad, as manifested by an extracted full width at half maximum (FWHM) value of 97 meV. To further improve QD uniformity, future efforts will focus on optimizing the strain conditions beneath the QDs and within the capping layers to achieve more consistent dot size and height. In Fig. 2(f), a shoulder near 1320 nm is observed in the spectrum without GaAs IL, which originates from interface-related type-II transition at the InP/InAlGaAs heterointerface. This was confirmed by PL measurement of a reference sample without the QD layer stack (Supplement 1 Fig. S1). This feature is suppressed in the spectrum with the GaAs IL due to enhanced QD emission. Given the improvements in dot morphology and PL intensity, we adopted the QD with the GaAs IL for the full 7-layer active region used in the laser structure shown in Figs. 2(a)–2(c).

3. Results and conclusion

The optimized InAs/InP QD structure was then fabricated into deep-etched ridge waveguide lasers. As illustrated in Fig. 3(a), the ridge was patterned and etched using inductively-coupled plasma (ICP) with SiN serving as the etch mask. Smooth and vertical sidewalls were obtained. The etch depth was controlled to extend below the QD active region, fully enclosing the gain medium within the ridge. In quantum well lasers, shallow-etched ridges are often used to prevent damage to the active region and reduce nonradiative surface recombination. Alternatively, wider ridges may be employed to limit current spreading and sidewall-related loss. In contrast, QD gain medium benefit from zero-dimensional carrier confinement, which significantly reduces in-plane carrier diffusion and sensitivity to sidewall defects [36]. Taking advantage of this, we adopted a deep-etched ridge geometry with a narrow 4 μm width. This structure enables strong lateral confinement of both carriers and optical modes, thereby suppressing higher-order transverse modes and improving beam quality.

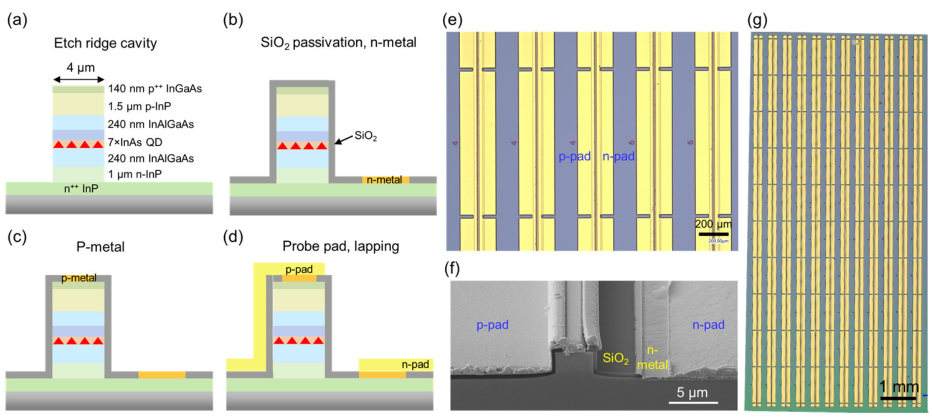

Fig. 3. Schematic of the fabrication process for the deep-etched ridge laser: (a) Ridge etching below the QD active region, (b) SiO_2 patterning and n-metal deposition, (c) p-metal deposition, and (d) probe pad deposition and substrate thinning. (e, g) Optical microscope images of the fabricated lasers after substrate thinning. (f) Cross-sectional SEM image of the cleaved laser bar, showing a smooth and mirror-like facet.

A top-top metal contact configuration was applied to the ridge waveguide laser. As illustrated in Fig. 3(b), following the ridge cavity etching, a 500 nm SiO_2 passivation layer was deposited by plasma-enhanced chemical vapor deposition (PECVD). Subsequently, the n-metal contact was formed on the exposed n-InP layer by e-beam evaporation of GeAu/Ni/Au (100/28/100 nm). Afterwards, as shown in Fig. 3(c), the p-metal contact was deposited on the p-InGaAs layer using a Ti/Pt/Au (10/20/300 nm) metal stack, followed by rapid thermal annealing at 385 °C for 3

Optics EXPRESS

minutes under nitrogen ambient to form ohmic contact. Next, as depicted in Fig. 3(d), probe pads (n-pad and p-pad) were deposited by Ti/Au (30/750 nm) sputtering to facilitate electrical probing. The backside of the substrate was then thinned down to a thickness of approximately 150 μm by mechanical lapping. Finally, the sample was cleaved into individual laser bars with varying cavity lengths for subsequent testing. No facet coating was applied. Microscope images presented in Figs. 3(e) and 3(g) show the device surfaces after substrate thinning, revealing clean surfaces with minimal defects such as hillocks or particles, thereby demonstrating excellent large-area uniformity in both epitaxial growth and fabrication processes. The cross-sectional SEM image of Fig. 3(f) illustrates the fabricated laser bar, showing mirror-like laser facets.

The electrical injection was performed using a pulse source (1 μs pulse width and 1% duty cycle). Fig. 4(a) shows a representative light-current (L–I) characteristic of a laser with a 4 μm × 500 μm cavity, yielding a threshold current of 20 mA. Low threshold currents of 17 mA for 300 μm cavity length and 28 mA for 1000 μm cavity length were also demonstrated at room temperature. To the best of our knowledge, the threshold currents achieved here represent one of the lowest values reported to date [29]. Fig. 4(b) presents a representative current–voltage (I–V) curve of a 4 μm × 500 μm laser, showing a turn-on voltage of approximately 0.7 V and on-resistance of 4 Ω.

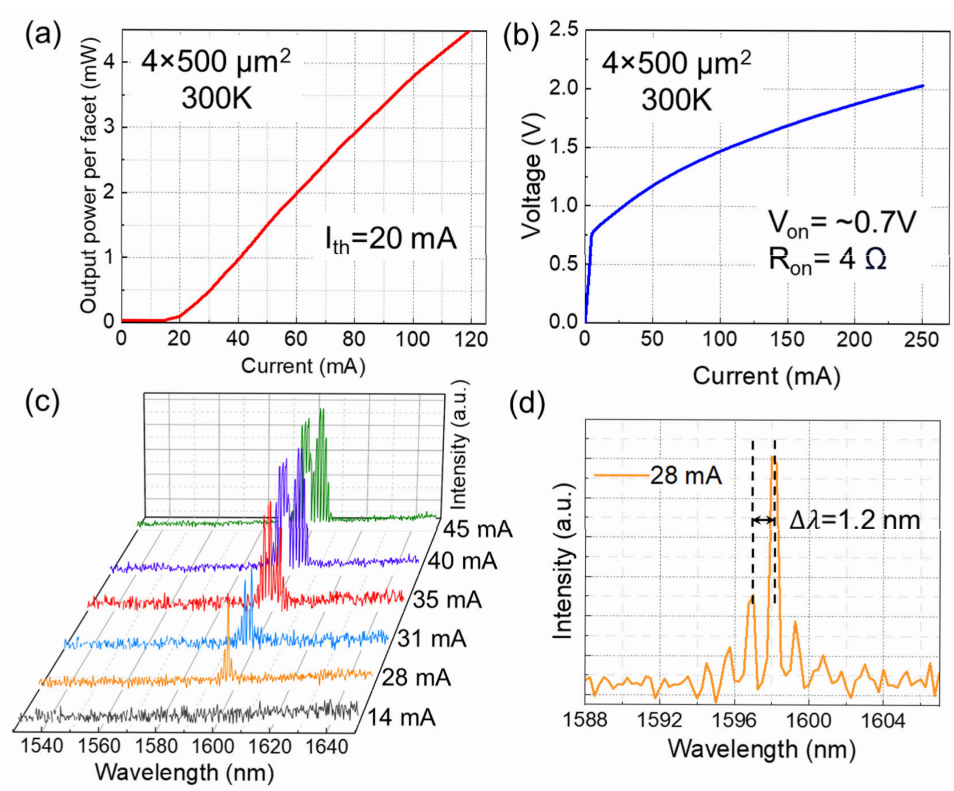

Fig. 4. (a) Light–current (L–I) characteristic of a laser with 4 μm ridge width and 500 μm ridge length, with an extracted threshold current of 20 mA. (b) Current–voltage (I–V) curve of a 4 μm × 500 μm laser. (c) Emission spectra of a 4 μm × 300 μm laser at room temperature under different injection currents. (d) Enlarged spectrum at 28 mA injection current, showing a longitudinal mode spacing of 1.2 nm.

Optics EXPRESS

More device measurements revealed a high yield of >98%, with only one device failing to achieve lasing among over 50 tested devices. Representative threshold currents and corresponding L–I curves of 12 devices are provided in Supplement 1 Fig. S2, illustrating the typical range and trend of the threshold currents for varied cavity lengths. For devices with a 4 µm ridge width, the maximum output power was measured to be approximately 6.5 mW for a 300 µm-long cavity and exceeded 8 mW for a 500 µm-long cavity (Supplement 1 Fig. S2). The lower slope efficiency observed for longer cavity devices is partially attributed to their lasing wavelengths approaching the cut-off limit of the InGaAs detector (800–1650 nm) used in our measurement set-up.

The emission spectra of the fabricated lasers were measured by coupling the output light into an optical spectrum analyzer using an optical fiber. Fig. 4(c) shows the emission spectra of a 4 µm × 300 µm laser under various injection currents. The threshold current of this device was measured to be 22.5 mA (see Supplement 1 Fig. S2). At an injection current of 28 mA, there is a dominant lasing peak. With further increase in injection currents, additional longitudinal modes begin to emerge. The redshift between the PL emission in Fig. 2(f) and the lasing wavelengths can be attributed to several factors. First, from single QD layer to the 7-layer QD structure, we observed a redshift of the PL emission due to the strain. Second, carrier-induced bandgap renormalization under electrical injection can lead to a redshifted gain spectrum. Moreover, the lower energy states are more easily to be inverted, which means the threshold condition may be reached at a wavelength which is longer than the PL peak. Fig. 4(d) plots the positions of the lasing peaks, revealing a longitudinal mode free spectrum range (FSR) of 1.2 nm. This corresponds to an average group index of $n_g = 3.55$, calculated using the relation $\Delta\lambda = \lambda^2/2n_gL$, where $L = 300\,\mu m$ is the cavity length. These results clearly confirm Fabry–Pérot (FP) lasing oscillations within the deep-etched ridge laser cavity.

Fig. 5(a) presents the light–current density (L–J) curves for devices with varied cavity lengths from 300 to 2000µm. A low threshold current density (J_{th}) of 630 A/cm^2 was obtained for the 2000µm cavity. Fig. 5(b) plots the J_{th} as a function of the inverse cavity length (1/L) extracted from Fig. 5(a). From the linear fit, a transparency current density (J_{tr}) of 440 A/cm^2 was extracted.

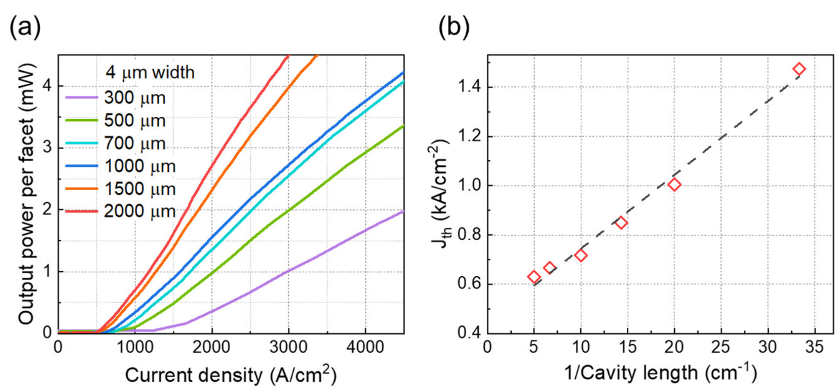

Fig. 5. (a) Light–current density (L-J) characteristics of lasers with 4 µm ridge width and varied ridge lengths from 300 µm to 2000 µm. (b) Threshold current density (J_{th}) plotted as a function of the inverse cavity length (1/L).

To evaluate thermal stability, temperature-dependent light–current measurements were carried out by varying the heat sink temperature. As a representative example, a 4 µm × 500 µm device was tested, and lasing was sustained up to 120 °C, as shown in Fig. 6(a). At elevated temperatures, both slope efficiency degradation and threshold current increase were observed. This behavior is commonly seen in semiconductor lasers due to increased nonradiative losses and reduced gain efficiency at higher temperatures. Specifically, the threshold current of the 4 µm × 500 µm laser increased from 25 mA at 20 °C to 145 mA at 120 °C. Fig. 6(b) shows the extracted threshold current values as a function of temperature, from which the characteristic temperature T_0 was derived using the relation: $\frac{I_{th}\ (T_1)}{I_{th}\ (T_2)} = \exp\left(\frac{T_1 - T_2}{T_0}\right)$. Over the moderate temperature range from 20 °C to 90 °C, characteristic temperature T_0 remains relatively stable at 74.9 K, indicating reasonable thermal robustness. However, at temperatures of 100 °C and above, T_0 drops to 34.5 K, suggesting that thermally activated losses become increasingly dominant in this high-temperature regime.

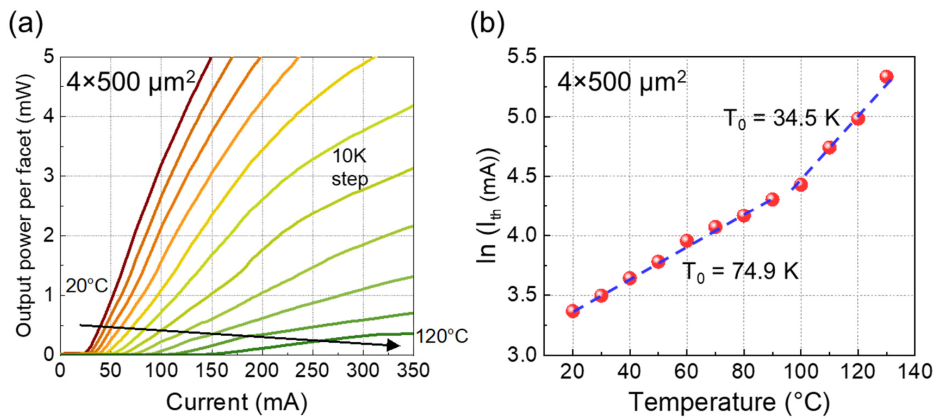

Fig. 6. (a) Temperature-dependent L–I characteristics of a 4 µm × 500 µm laser. (b) Threshold current as a function of heat sink temperature for the same device. A characteristic temperature T_0 of 74.9 K was extracted in the range of 20 °C to 90 °C, and 34.5 K from 100 °C to 120 °C.

In preliminary experiments, several devices were tested under continuous-wave (CW) electrical injection, and CW lasing was achieved at room temperature. A 4 µm × 3000 µm device exhibited CW lasing with a threshold current of approximately 120 mA, as compared to a threshold current of 60 mA under pulsed injection. More effort is needed to improve the CW performance at elevated temperatures.

4. Conclusion

In conclusion, we have demonstrated low-threshold-current and high-yield InAs/InP QD lasers grown by MOCVD. Deep-etched ridge waveguide lasers were fabricated with a narrow 4 µm ridge width and top–top metal contact configuration. The devices achieved threshold currents of 17 mA for 300 µm cavity length and 28 mA for 1000 µm cavity length. Lasing operation was maintained up to 120 °C. These results confirm the potential of MOCVD-grown InAs/InP QD lasers as light sources for the C- and L-band applications and for future integration on silicon platforms.

Funding. Engineering and Physical Sciences Research Council (EP/V029681/1, EP/V029606/1, EP/V055224/1); UK Research and Innovation (UKRI) Strength in Places Fund (Grant Number 107134).

Disclosures. The authors declare no conflict of interest.

Data availability. Data supporting the findings of this study are available at [37].

Supplemental document. See Supplement 1 for supporting content.

References

1. M. Smit, X. Leijtens, H. Ambrosius, *et al.*, "An introduction to InP-based generic integration technology," Semicond. Sci. Technol. **29**(8), 083001 (2014).

2. M. Smit, K. Williams, and J. v. d. Tol, “Past, present, and future of InP-based photonic integration,” APL Photonics **4**(5), 050901 (2019).
3. M. Cantono, R. Schmogrow, M. Newland, *et al.*, “Opportunities and Challenges of C + L Transmission Systems,” J. Lightwave Technol. **38**(5), 1050–1060 (2020).
4. V. Lopez, B. Zhu, D. Moniz, *et al.*, “Optimized Design and Challenges for C&L Band Optical Line Systems,” J. Lightwave Technol. **38**(5), 1080–1091 (2020).
5. B. J. Isaac, B. Song, S. Pinna, *et al.*, “Indium Phosphide Photonic Integrated Circuit Transceiver for FMCW LiDAR,” IEEE J. Sel. Top. Quantum Electron. **25**(6), 1–7 (2019).
6. S. Arafin and L. A. Coldren, “Advanced InP Photonic Integrated Circuits for Communication and Sensing,” IEEE J. Sel. Top. Quantum Electron. **24**(1), 1–12 (2018).
7. Z. Yan, Y. Han, L. Lin, *et al.*, “A monolithic InP/SOI platform for integrated photonics,” Light: Sci. Appl. **10**(1), 200 (2021).
8. S. Chen, W. Li, J. Wu, *et al.*, “Electrically pumped continuous-wave III–V quantum dot lasers on silicon,” Nat. Photonics **10**(5), 307–311 (2016).
9. F. Grillot, J. Duan, B. Dong, *et al.*, “Semiconductor quantum dot lasers: Genesis, prospects, and challenges,” In *Photonic Materials and Applications Series, Quantum Photonics*, Elsevier, 2024, Pages 191–266, ISBN 780323983785, https://doi.org/10.1016/B978-0-323-98378-5.00008-8.
10. J. Duan, H. Huang, B. Dong, *et al.*, “1.3-μm Reflection Insensitive InAs/GaAs Quantum Dot Lasers Directly Grown on Silicon,” IEEE Photonics Technol. Lett. **31**(5), 345–348 (2019).
11. B. Dong, M. Dumont, O. Terra, *et al.*, “Broadband quantum-dot frequency-modulated comb laser,” Light: Sci. Appl. **12**(1), 182 (2023).
12. Z. Liu, C. Hantschmann, M. Tang, *et al.*, “Origin of Defect Tolerance in InAs/GaAs Quantum Dot Lasers Grown on Silicon,” J. Lightwave Technol. **38**(2), 240–248 (2020).
13. C. Shang, E. Hughes, Y. Wan, *et al.*, “High-temperature reliable quantum-dot lasers on Si with misfit and threading dislocation filters,” Optica **8**(5), 307–311 (2021).
14. Y. Han, H. Park, J. Bowers, *et al.*, “Recent advances in light sources on silicon,” Adv. Opt. Photonics **14**(3), 404–454 (2022).
15. R. Koscica, A. Skipper, B. Shi, *et al.*, “Quantum Dot DBR Lasers Monolithically Integrated on Silicon Photonics by In-Pocket Heteroepitaxy,” J. Lightwave Technol. **43**(12), 5773–5781 (2025).
16. W. Q. Wei, A. He, B. Yang, *et al.*, “Monolithic integration of embedded III-V lasers on SOI,” Light: Sci. Appl. **12**(1), 84 (2023).
17. Z. Yan and Q. Li, “Recent progress in epitaxial growth of dislocation tolerant and dislocation free III–V lasers on silicon,” J. Phys. D: Appl. Phys. **57**(21), 213001 (2024).
18. Y. Xue, W. Luo, S. Zhu, *et al.*, “1.55 μm electrically pumped continuous wave lasing of quantum dash lasers grown on silicon,” Opt. Express **28**(12), 18172–18179 (2020).
19. B. Shi, S. Pinna, W. Luo, *et al.*, “Comparison of static and dynamic characteristics of 1550 nm quantum dash and quantum well lasers,” Opt. Express **28**(18), 26823–26835 (2020).
20. R. J. Chu, T. Laryn, D. H. Ahn, *et al.*, “Low-threshold 2 μm InAs/InP quantum dash lasers enabled by punctuated growth,” Opt. Express **32**(2), 1334–1341 (2024).
21. M. Z. M. Khan, T. K. Ng, and B. S. Ooi, “Self-assembled InAs/InP quantum dots and quantum dashes: Material structures and devices,” Prog. Quantum Electron. **38**(6), 237–313 (2014).
22. S. Banyoudeh, A. Abdollahinia, O. Eyal, *et al.*, “Temperature-Insensitive High-Speed Directly Modulated 1.55-μm Quantum Dot Lasers,” IEEE Photonics Technol. Lett. **28**(21), 2451–2454 (2016).
23. A. Abdollahinia, S. Banyoudeh, A. Rippien, *et al.*, “Temperature stability of static and dynamic properties of 1.55 μm quantum dot lasers,” Opt. Express **26**(5), 6056–6066 (2018).
24. D. Jung, D. J. Ironside, S. R. Bank, *et al.*, “Effect of growth interruption in 1.55 μm InAs/InAlGaAs quantum dots on InP grown by molecular beam epitaxy,” J. Appl. Phys. **123**(20), 205302 (2018).
25. J. Kwoen, N. Morais, W. Zhan, *et al.*, “All III-arsenide low threshold InAs quantum dot lasers on InP(001),” Electron. Lett. **59**(16), e12920 (2023).
26. H. Jia, X. Yu, T. Zhou, *et al.*, “Long-wavelength InAs/InAlGaAs quantum dot microdisk lasers on InP (001) substrate,” Appl. Phys. Lett. **122**(11), 111108 (2023).
27. J. Yuan, C. Dear, H. Jia, *et al.*, “Indium-flush technique for C-band InAs/InP quantum dots,” APL Mater. **12**(12), 121109 (2024).
28. J. Kwoen, M. Kakuda, and Y. Arakawa, “Wide-range emission wavelength control of InAs quantum dots by changing the indium composition in an InAlGaAs capping layer,” Opt. Mater. Express **15**(4), 939–948 (2025).
29. J. S. Park, H. Jia, H. Zeng, *et al.*, “Low threshold InAs/InP quantum dot lasers,” Opt. Express **33**(9), 19158–19165 (2025).
30. S. Zhu, B. Shi, Q. Li, *et al.*, “1.5 μm quantum-dot diode lasers directly grown on CMOS-standard (001) silicon,” Appl. Phys. Lett. **113**(22), 221103 (2018).
31. Y. Koninck, C. Caer, D. Yudistira, *et al.*, “GaAs nano-ridge laser diodes fully fabricated in a 300-mm CMOS pilot line,” Nature **637**(8044), 63–69 (2025).
32. R. Alcotte, M. Martin, J. Moeyaert, *et al.*, “Epitaxial growth of antiphase boundary free GaAs layer on 300 mm Si(001) substrate by metalorganic chemical vapour deposition with high mobility,” APL Mater. **4**(4), 046101 (2016).

Optics EXPRESS

33. S. Liu, B. Ratiu, M. Tang, *et al.*, "Effective InAsP dislocation filtering layers for InP heteroepitaxy on CMOS-standard (001) silicon," Appl. Phys. Lett. **125**(8), 082102 (2024).
34. Y. Han, Z. Yan, Y. Xue, *et al.*, "Micrometer-scale InP selectively grown on SOI for fully integrated Si-photonics," Appl. Phys. Lett. **117**(5), 052102 (2020).
35. C. Shang, K. Feng, E. Hughes, *et al.*, "Electrically pumped quantum-dot lasers grown on 300 mm patterned Si photonic wafers," Light: Sci. Appl. **11**(1), 299 (2022).
36. C. Shang, Y. Wan, J. Selvidge, *et al.*, "Perspectives on Advances in Quantum Dot Lasers and Integration with Si Photonic Integrated Circuits," ACS Photonics **8**(9), 2555–2566 (2021).
37. Z. Yan, S. Liu, B.-P. Ratiu, *et al.*, "MOCVD-grown InAs/InP quantum dot lasers with low threshold current: data," Cardiff University Research Data, 2025, https://doi.org/10.17035/cardiff.29293718